Investigation of thermally activated deformation in amorphous PMMA and Zr-Cu-Al bulk metallic glasses with broadband nanoindentation creep

J.B. Puthoff
Materials Science Program, University of Wisconsin–Madison, Madison, Wisconsin 53706

J.E. Jakes
Materials Science Program, University of Wisconsin–Madison, Madison, Wisconsin 53706; and USDA Forest Product Laboratory, Madison, Wisconsin 53726

H. Cao
Materials Science Program, University of Wisconsin–Madison, Madison, Wisconsin 53706

D.S. Stone [a)]
Materials Science Program, University of Wisconsin–Madison, Madison, Wisconsin 53706; and Materials Science and Engineering, University of Wisconsin–Madison, Madison, Wisconsin 53706

(Received 2 August 2008; accepted 11 December 2008)

The development of nanoindentation test systems with high data collection speeds has made possible a novel type of indentation creep test: broadband nanoindentation creep (BNC). Using the high density of data points generated and analysis techniques that can model the instantaneous projected indent area at all times during a constant-load indentation experiment, BNC can reveal materials properties across a range of strain rates spanning up to five decades (10^{-4}–$10\ s^{-1}$). BNC experiments aimed at measuring activation parameters for plasticity were conducted on three systems: two Zr-based bulk metallic glasses and poly-(methyl methacrylate) (PMMA). The results give insight into the operation of the deformation mechanisms present in the test materials, including the dependence of the deformation rate on the hydrostatic component of the stress for PMMA and the form of the activation energy function for the metallic glasses.

I. INTRODUCTION

Instrumented indentation techniques for determining the hardness and elastic moduli of materials have been applied across a wide range of scientific disciplines. These techniques have proved useful in investigations of metallic, ceramic, polymeric, and biological materials,[1] and the development of high-resolution indentation (nanoindentation)[2–4] has allowed these types of measurements to be conducted on specimens whose geometries or properties disallow other testing techniques (e.g., thin films, complex biologicals, phases in alloys, brittle materials). Less well-known, but equally important, are the uses of instrumented indentation for measuring the temperature- and strain-rate-dependent (creep) properties of materials.[5–10] These properties provide information on the kinetics of plastic deformation and the operation of the underlying mechanisms.

In this paper, we present a new nanoindentation creep technique, broadband nanoindentation creep (BNC), which is capable of determining activation parameters for low-temperature deformation from a single, room temperature experiment. This new technique is made possible by (i) the high data collection rates found on current-generation nanoindenters and (ii) a mathematical model that can assess the instantaneous indent size at all times during the experiment. From a BNC experiment, in which the indenter is brought to some specified level of load (P_{max}) and held for a prescribed period (the creep time, t_{creep}), we can construct a hardness versus indentation strain rate [$H(\dot{\varepsilon}_H)$] curve. BNC curves typically span more than four decades of strain rate and can be analyzed to probe the kinetic processes that govern deformation.

In the nanoindentation literature, hardness is usually represented as if it were rate- and time-independent. This is not wholly appropriate, because even a cursory examination reveals the indenter slowly creeps into the material if held at maximum load (i.e., the usual nanoindentation hardness depends on how long the indenter is held in the material). This creep can be discerned not only in the usual materials—polymers near the glass transition or metals at high temperature—but also in hard and brittle materials like quartz.[11] With BNC, it is possible to explicitly track the rate- and time-dependence of the hardness as the area grows beneath the indenter. The

[a)]Address all correspondence to this author.
e-mail: dsstone@wisc.edu
DOI: 10.1557/JMR.2009.0145

instantaneous hardness [$H(t)$] measured in BNC approaches the normal "static" nanoindentation hardness at the end of the creep test. At any time before the end of the creep test, the instantaneous hardness is what the nanoindentation hardness would be if the creep test were interrupted at that time.

Low-temperature deformation mechanisms in crystalline materials are well-studied.[12,13] Plastic deformation in metallic glasses, particularly in the low-temperature regime, is still imperfectly understood. Additionally, plasticity in polymers subjected to indentation has not been given thorough consideration. We have therefore chosen to use two Zr-based bulk metallic glasses (BMGs), $Zr_{54}Cu_{38}Al_8$ ("Zr54") and $Zr_{45}Cu_{49}Al_6$ ("Zr45"), and amorphous poly-(methyl methacrylate) (PMMA) as our test systems. The mechanism by which each of these materials deforms at low temperatures is expected to be thermally activated, with a stress-dependent activation energy.[14,15]

II. BACKGROUND

A. Thermally activated flow and associated activation parameters

The deformation produced in a material by the operation of a given mechanism is determined by a constitutive law[12]:

$$\dot{\varepsilon}_{ij} = \dot{\varepsilon}_{ij}(\sigma, T, \text{structure}) \quad , \tag{1}$$

where $\dot{\varepsilon}_{ij}$ is a component of the strain rate tensor, σ is the applied stress tensor, and T is the temperature. Plastic deformation is typically driven primarily by shear stresses (τ), but can be affected by the hydrostatic stress [$\sigma_h = \text{tr}(\boldsymbol{\sigma})/3$]. The structural parameters depend on such details as: atomic scale organization, defect structure, defect density, and the organization of superstructural units (such as grains). These parameters may vary for otherwise similar specimens according to deformation history and heat treatment, but they are typically taken to be constant during low-temperature deformation (the "isostructural assumption"), or to be entirely dependent on the temperature and stress level at high temperatures.[12] Constitutive laws are frequently phenomenological in origin, and devising experimental techniques for determining the material-dependent parameters is of significant importance to materials scientists.

During low-temperature deformation, many materials exhibit Arrhenius-type flow behavior, for which Eq. (1) can be written as[16]

$$\dot{\varepsilon} = \dot{\varepsilon}_0 \exp\left[-\frac{\Delta G(\sigma)}{k_B T}\right] \quad , \tag{2}$$

where $\dot{\varepsilon}_0$ is a material-, stress-, and structure-dependent rate parameter, ΔG is the activation energy for the operation of the underlying elementary rate process, and k_B is Boltzmann's constant. $\dot{\varepsilon}_0$ is proportional to the concentration of elementary defects which produce plastic strain.[12] Most of the sensitivity of strain rate to stress enters through the ΔG term.

The derivative of ΔG with respect to some component (or components) of σ can be expressed in terms of an activation volume (V^*). Because both shear and hydrostatic stresses are present in a hardness test, it is useful to work with a collection of activation volumes, defined by

$$V_\tau^* \equiv k_B T \left.\frac{\partial \ln \dot{\varepsilon}}{\partial \tau}\right|_{\varepsilon,T,\sigma_h} (\text{shear stress}) \quad , \tag{3a}$$

$$V_\tau^* \equiv k_B T \left.\frac{\partial \ln \dot{\varepsilon}}{\partial \sigma_h}\right|_{\varepsilon,T,\tau} (\text{hydrostatic stress}) \quad , \tag{3b}$$

$$V_\tau^* \equiv M k_B T \left.\frac{\partial \ln \dot{\varepsilon}}{\partial \sigma}\right|_{\varepsilon,T} (\text{uniaxial stress}) \quad . \tag{3c}$$

The derivatives are taken at fixed strain to avoid changes in structure that arise from work hardening or softening. Equations (3a) and (3b) describe, respectively, the effects of shear and hydrostatic stress on the activation energy in Eq. (2), as $V_\tau^* \approx -\partial \Delta G/\partial \tau$ and $V_\tau^* \approx -\partial \Delta G/\partial \sigma_h$. Equation (3c) refers to the influence of the stress in a uniaxial experiment (σ), which mixes shear and hydrostatic stresses. M is a factor relating uniaxial stress to the shear stresses that operate the defects. The parameters V_τ^* and V_h^* are most fundamental, but V_σ^* is usually easiest to measure. In the absence of any effect of hydrostatic stress on strain rate, V_σ^* should equal V_τ^*.

Bulk metallic glasses lack a crystalline structure and deform by mechanisms other than conventional dislocation glide/climb or grain-sliding.[17,18] Deformation in metallic glasses is believed to be produced by the ensemble rearrangement of groups of 50–100 atoms, called shear transformation zones (STZs).[19,20] The irreversible, low temperature deformation of an STZ is similar in operation to an Eshelby inclusion.[21] To make the transition to its sheared state, an STZ must overcome an activation barrier (ΔG_{STZ}), which has been taken to be of the form[14]

$$\Delta G_{STZ} = \Delta G_0 \left(\frac{\tau_c - \tau}{\tau_c}\right)^n \quad , \tag{4}$$

where ΔG_0 is the activation energy required at zero stress, τ_c is the flow stress at $T = 0$ K, and n is the power law exponent describing the shape of the activation barrier. $n = 1$,[17] 2,[19] and 3/2[14] have been predicted. The deformation produced in a BMG is proportional to the rate of activation of individual STZ flow units, in accordance with Eq. (2). Plasticity in PMMA is believed to proceed by a combination of the α- and β-relaxation processes, in which the coupled motions of the main

chains (α) and side groups (β) produce the observed deformation.[22,23]

Common to plastic deformation in both BMGs and PMMA are the dilatational effects that accompany the operation of the low-temperature mechanism. In the case of the BMG, the activation of an STZ produces an increase in free volume[19] around the STZ, much like the local dilatation observed in the shear deformation of granular materials.[24] For PMMA, deformation also appears to produce localized volumetric changes.[22] These dilatency effects will have an influence on test data. During nanoindentation creep, the material under the indenter is constrained and experiences a compressive hydrostatic stress. The operation of the deformation mechanism must do work against this stress,[25] equivalent to $\sigma_h V_h^*$, where V_h^* is the average change in volume of the flow unit.

The production and annihilation of free volume during deformation is expected to alter the structure of the MG and thereby change the parameters in Eq. (2),[17,19] but the associated defect production should saturate and defect annihilation rates should vanish as the material approaches a steady state at high strain rates and low temperatures.[19] Under these conditions, the constitutive behavior of the material will reflect the ideal, isostructural case. The fact that inhomogeneous deformation is often observed in the form of shear bands does not contradict this idea; it merely shows that two different structures coexist: a deformed structure that has been softened by virtue of the excessive accumulation of free volume, and an undeformed region that is comparatively hard.

B. Characterization of thermally activated flow with indentation creep

In indentation creep, the indenter is pushed into the specimen until a predetermined load is reached, at which point the load is held constant. Under the influence of this load, the indenter continues to penetrate at a rate determined by the plastic flow properties of the material, and the area of the indent increases. This increase produces a decrease in the average pressure, or hardness, beneath the indenter. The instantaneous hardness is defined as the instantaneous load divided by the instantaneous projected area, or

$$H(t) \equiv \frac{P(t)}{A(t)} \quad . \tag{5}$$

This instantaneous hardness is a measure of the instantaneous flow stress of the material. We can also identify an indentation strain rate ($\dot{\varepsilon}_H$) in the deforming material at any time during the experiment, given by[26]

$$\dot{\varepsilon}_H(t) \equiv \frac{\mathrm{d}\,\ln\sqrt{A}}{\mathrm{d}t} \quad . \tag{6}$$

As the creep experiment progresses, the indent expands less rapidly, and the strain rate decreases. Physically, $\dot{\varepsilon}_H$ represents an "average" strain rate in the plastic zone beneath the indenter.[26] There is a distribution of strain rates in the plastic zone, but this distribution scales with $\dot{\varepsilon}_H$.

The activation volumes in Eqs. (3a)–(3c) entail derivatives of the strain rate with respect to stress. We discuss these derivatives in terms of their inverses, the strain rate sensitivity parameters (m_σ and m_τ) given by

$$m_\sigma \equiv \left.\frac{\partial\,\ln\sigma}{\partial\,\ln\dot{\varepsilon}}\right|_{\varepsilon,T} \quad , \tag{7a}$$

and

$$m_\tau \equiv \left.\frac{\partial\,\ln\tau}{\partial\,\ln\dot{\varepsilon}}\right|_{\varepsilon,T} \quad . \tag{7b}$$

m_σ and m_τ can be measured in a displacement-controlled experiment by deforming the material to a specified level of strain at one strain rate, then abruptly changing the strain rate and measuring the resulting change in stress. If yielding is unaffected by hydrostatic stress, then m_τ and m_σ should be equal. The strain rate sensitivity of the hardness is defined as

$$m_H \equiv \left.\frac{\partial\,\ln H}{\partial\,\ln\dot{\varepsilon}_H}\right|_{h_p,T} \quad , \tag{7c}$$

where the partial derivative is taken at constant indent depth to exclude the effects of an indentation size effect, if any. Finite element analysis simulations have revealed that, for von Mises solids, m_H/m_σ is a unique function of the hardness/modulus ratio.[26]

C. Broadband nanoindentation creep

Broadband nanoindentation creep is a creep test in which the full dynamic range of the experimental apparatus is used to measure material properties over the widest range of strain rates possible. For the Hysitron (Minneapolis, MN) Triboindenter, the high frequency response of the instrument is limited by the low-pass filter on the displacement signal, with a roll-off frequency of 1000 Hz. The data collection rate exceeds 1000 points per second. In practice, we find that we can reliably achieve strain rates of greater than 10 s^{-1} by using loading times less than 0.05 s. The low strain rate limit is dictated by uncertainties in thermal drift, but is typically about 10^{-4} s^{-1}.

In what follows, we examine the kinetics of deformation during indentation in PMMA and two different Zr-Cu-Al BMGs using broadband nanoindentation creep. It is evident from Eqs. (5) and (6) that a key component in the analysis of BNC data is to identify how the area of the indent increases with time during creep. Special attention is paid to this aspect of the analysis, which combines a simple model of indenter penetration[8] with

relations determined from a finite element analysis simulation of indentation creep.[26,27]

III. EXPERIMENTAL WORK

A. Materials

The Zr54 and Zr45 BMGs were suction-cast[28] in a water-cooled copper mold from a melt of pure components at the University of Wisconsin–Madison. The ingot diameters were 3 mm, and a piece 3 mm in length was taken from each near the bottom of the ingot (where the highest quench rates exist) for BNC measurements. Another piece of each ingot, contiguous to the BNC specimen, was taken for XRD, DSC, and TEM analysis to verify the glassy nature of the ingot.[29] We mechanically polished one face of each specimen to a mirror finish, both to remove any surface oxides and to produce a flat, perpendicular surface for indentation. The PMMA specimen was a nanoindentation standard obtained from Hysitron Inc. and was tested in the as-received condition.

B. Nanoindentation experiments

We conducted all experiments on a Hysitron Triboindenter with a Quesant (Agoura Hills, CA) atomic force microscope (AFM) attachment. The electronics package of this instrument provides the data-collection rates required for BNC measurements when the instrument is operated in "open loop" mode and set to record the maximum possible number of data points (≈132,000). Indentation creep tests were performed overnight following setup the previous day. Drift was assessed using two methods, described below. Typical rates of drift were less than 0.05 nm/s, and they tended to vary only slowly from one test to the next.

The BMG specimens were each subjected to three different series of eight BNC tests. For each series, a different peak load was specified: P_{max} = 10, 5, or 2.5 mN. In the individual tests, the indenter tip/specimen was loaded to the given P_{max} in 0.05 s, held for a prescribed period: t_{creep} = 0.01, 0.05, 0.1, 0.5, 2, 10, or 50 s, and unloaded. The unloading times (t_{unload}) varied between tests; they were as brief as 0.01 s (for t_{creep} = 0.01 s) or 0.05 s (for t_{creep} = 0.1 and 0.5 s) and as long as 0.5–1 s (for t_{creep} = 2, 10, 50 s). We performed two tests with t_{creep} = 0.05 s, one with t_{unload} = 0.05 s and the other with t_{unload} = 0.01 s, to assess the effects of electronic filtering on the test data. In the tests for which t_{creep} was 0.5 s or greater, the unloading segment of the experiment was halted at 20% of P_{max} and allowed to dwell at this load for an interval between 6 and 50 s. We used the data collected during this portion to determine thermal drift corrections for the instrument.

To investigate whether or not the indentation creep properties depend on the deformation history, the Zr54 specimen was subjected to supplementary tests in addition to the BNC experiments. For these supplementary experiments, loading, hold, and unloading segments had equal duration. For each series of indents, at P_{max} = 10, 5, or 2.5 mN, we conducted tests with load/hold/unload times of 0.05 s, 0.5 s, and 50 s. We included dwell times at 20% of P_{max} of 6 s and 100 s for the 5 s and 50 s tests, respectively.

BNC tests were also conducted on the PMMA. We subjected the material to three series of tests, each at different loads (10, 5.8, and 1.6 mN). Each series consisted of 8 indents, all with the same loading and unloading segments (0.1 s for both) but with different hold times (0.01, 0.05, 0.1, 0.2, 0.5, 1, 10, and 50 s). Drift was calculated using the procedures that came with the instrument, which consists of holding the indenter tip in contact with a force of 1 μN for 200 s prior to an indent and fitting a straight line to the last 50 s of this hold.

C. Imaging of the indents

Following the nanoindentation experiments, we imaged the residual indents with the AFM attachment. Scans were performed in contact mode, with a scan range of 4 × 4 μm for the indents on the BMG specimens and 10 × 10 μm for the indents in PMMA. The instrument was calibrated for each range with a standard of pitch 292 ± 0.5 nm, acquired from Advanced Surface Microscopy, Inc. (http://www.asmicro.com). ImageJ image analysis software (http://rsb.info.nih.gov/ij/) was used to determine the residual indent areas, following Jakes et al.[30] For the BMGs, we found the best way to identify the projected area of contact was to rely on an abrupt change in the slope of the surface to represent the edge of contact rather than relying on height information alone.

D. Correction of the displacement signal to take into account filters

In addition to correction for drift, a second correction is necessary to account for the electronic filters that reduce noise in the displacement signal. To illustrate the effects of these filters, Fig. 1(a) shows the raw load-displacement data for two tests conducted on the Zr45 BMG specimen at P_{max} = 10 mN. Both tests have the same loading and hold segments (0.05 s for each segment), but the unloading segments are different: t_{unload} = 0.05 s and 0.01 s, respectively. The "nose" visible at the top of the unloading portion of each curve (indicated by arrows) is an artifact introduced by the electronics, and the shape of the nose is clearly influenced by the rate of unloading. Because the nose is much larger for the curve with faster unloading, we know that the nose cannot be caused by creep or anelastic relaxation, as sometimes reported in the literature.[31] Also, there is a similar artifact at the beginning of loading (again indicated by an arrow), in which the load appears to increase more

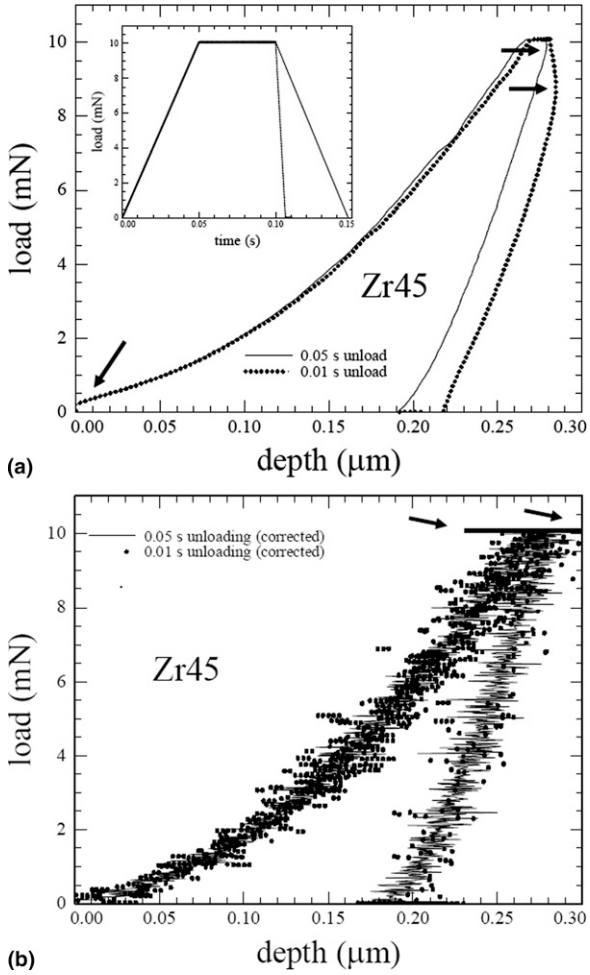

FIG. 1. Correction of load-depth traces for effects of filtering in displacement electronics: (a) uncorrected load-depth traces for 0.01 s and 0.05 s unloads. The two curves differ in the unloading segment due to the effects of the filter. Arrows point to "nose" artifacts in the data caused by filtering. (b) The corrected data are much more noisy, but the nose artifacts are removed to be replaced by sharp "overshoots" at the beginning and end of creep. These overshoot artifacts can be discarded from the analysis, and indentation strain rates and hardness can be calculated despite the noise.

rapidly with depth than it should. Both artifacts become more pronounced the faster the experiment is run.

On the Triboindenter, a second order low-pass filter is used to reduce noise on the displacement signal, and as such it is governed by a second order linear differential equation. The corrections to eliminate delays in the displacement signal brought about by this filter necessarily use the first and second derivatives of the displacement signal. If h_{meas} is the recorded displacement and h the actual displacement, then

$$h = h_{meas} + C_1 \frac{dh_{meas}}{dt} + C_2 \frac{d^2 h_{meas}}{dt^2} \quad , \qquad (8)$$

where C_1 and C_2 are constants determined by the frequency response of the filter. It is possible to adjust this filter, so we set it to the fastest response available, 1000 Hz. C_1 and C_2 for this filter were identified by finding the pair of values that takes the uncorrected load-displacement curves of Fig. 1(a) and gets them to overlap, as shown in Fig. 1(b). The determined values were 1.4 ($\pm$0.1) $\times$ 10^{-3} s and 8 ($\pm$1) $\times$ 10^{-7} s^2, respectively. We used these constants and Eq. (8) to correct all of the test data. When this correction is introduced, the noses seen in Fig. 1(a) disappear, only to be replaced by an overshoot (or sharp nose) at the highest load immediately prior to unloading in Fig. 1(b). This overshoot is caused by the large value of the second derivative in displacement encountered at the beginning of unloading. The second derivative is a delta function at this point, and Eq. (8) becomes singular. The overshoot part of the load-depth curve was discarded in all of the analyses, and therefore had little effect on any of the data. For the analysis of creep, the correction is most important for the highest strain rates encountered at the beginning of an experiment; even so, the highest decade of strain rate (>30 s^{-1}) was discarded because of inability to ensure accuracy there. Because the second and third terms in Eq. (8) are noisy, the correction produces a large amount of scatter in the corrected depth signal of Fig. 1(b). Despite their noise, the corrected nanoindentation traces can still be analyzed for creep, because the creep analysis entails least-squares fits to relatively long time intervals compared to the characteristic timescale of the noise.

E. Calculation of *A*(*t*)

From the corrected nanoindentation data, the hardness versus strain rate data for BNC may be extracted. The instantaneous hardness can be determined at all times during the creep portion of the indentation data using the method of Stone and Yoder.[8] This analysis has been supplemented by relations determined from finite element simulations.[26,27] In our analysis, H depends on the plastic component of the instantaneous indentation depth [$h_p(t)$] and the load. h_p can be written as

$$h_p(t) = h(t) - P(t)\left[\frac{1}{\beta E^* \sqrt{A(t)}} + C_m\right] \quad , \qquad (9)$$

where E^* is the effective modulus during indentation, and C_m is the machine compliance. $E^* = [(1 - \nu^2)/E + (1 - \nu_d^2)/E_d]^{-1}$, where $\{E, \nu\}$ and $\{E_d, \nu_d\}$ are {modulus, Poisson's ratio} of the test specimen and diamond, respectively. We find that the geometrical constant, β, is approximately 1.23.[30] $A(t)$, the instantaneous projected indent area, cannot be measured directly, and is typically assumed to be proportional to the square of depth.[32,33] As was recently shown,[27] this assumption breaks down for material with high H/E^*.

The key to analyzing the creep portion of the experiment for hardness and strain rate is to identify how A changes with h_p during the experiment prior to reaching

the final area, A_0. To the first order, $1/\sqrt{A} \approx 1/\sqrt{A_0}\left(1 - \Delta\ln\sqrt{A}\right)$, where $\Delta\ln\sqrt{A} \approx (A - A_0)/2A_0$ is the logarithmic change in $\sqrt{A}$. Formally, $\Delta\ln\sqrt{A}$ can be related to changes in the depth according to[27]

$$\Delta \ln \sqrt{A} \equiv \zeta_p \Delta \ln h_p \quad , \tag{10}$$

where ζ_p is a power law exponent and $\Delta\ln h_p \approx \left(h_p - h_{p0}\right)/h_{p0}$, where h_{p0} is the plastic depth at unloading.[34] The correct value of ζ_p can be inferred from the measured A_0 values taken from experiments with different creep times and depths. In general, ζ_p depends on the ratio H/E^*. For $H/E^* \ll 1$, ζ_p approaches 1, consistent with the area-depth relation for a pyramidal indenter. However, because of the effects of elastic displacements beneath the indent, ζ_p is generally not equal to 1.[27] In our test materials, the values of H/E^* at unloading are 0.06, 0.06, and 0.05 for the Zr54, Zr45, and PMMA, respectively.

Using Eq. (10), $A(t)$ in Eq. (9) can be expanded in a Taylor series in terms of h_p, then an expression for h_p can be obtained in terms of quantities that are known.[8] From the calculated h_p, we can construct A, H, and $\dot{\varepsilon}_H(t)$ for the creep region. Assuming for an experiment that ζ_p is constant, A becomes

$$A(t) = A_0 \exp\left[2\zeta_p \ln\left(\frac{h_p(t)}{h_{p0}}\right)\right] \quad . \tag{11}$$

By comparing the calculated change in area from this equation with the measured changes in area (obtained by interrupting creep after different intervals of time) we have found $\zeta_p = 0.95$ for the BMGs and $\zeta_p = 1.1$ for PMMA. In those simulations, ζ_p is found to differ from 1 because of the effects of H/E^* on pileup and sink-in,[27] which are therefore incorporated into the analysis in a systematic way. Because the previous simulations are for cones, it is not clear that predicted ζ_p should transfer over to experiments using Berkovitch indenters. We use ζ_p as a fitting parameter for analyzing our data, and adjust it so that the calculated area versus time profile agrees with the measured area versus time data. We find that $\zeta_p = 0.95$ measured for BMGs is close to $\zeta_p = 0.87$ predicted for cones in materials with the same H/E^* ratios. The measured ζ_p for PMMA (=1.1) is about 20% higher than predicted based on analysis with cones.

IV. RESULTS

A. PMMA experiments

The load-displacement curves collected for the PMMA sample are shown in Fig. 2 and illustrate the differences in depth achieved by allowing the constant load creep portion of the experiment to last for different lengths of time. The curves have been corrected for thermal drift and electronic filtering. The loading and unloading portions of the curves with longer creep times are seen to be serrated. These serrations are caused by the finite time-resolution of the software that controls the load. Changes in load take place at discrete time intervals, with a minimum interval equal to about 1/8000th of the total time of the experiment. In BNC experiments with long creep segments and short loading and unloading segments, the loading and unloading occur in a series of steps, rather than a smooth ramp. In principle, because of these large and abrupt changes in load, the strain rates achieved during loading in these experiments are higher than those achieved in experiments with shorter, constant load creep segments. Our ability to resolve those higher strain rates is limited because of the filtering of the displacement signal.

Images of the smallest and largest indents from creep experiments at 10 mN load are shown in Fig. 3. The corresponding creep times are 0.01 s and 50 s. During the interval between these times, the area increases by a factor of ~2.6. The contours identifying the contact edges used to determine the values of A_0 for the entire set of tests are shown in Fig. 3, at right. It is significant that the shape of the indent changes from a three-pointed star at short creep times (caused by the presence of sink-in) to more of a triangle at longer creep times (caused by the loss of sink-in as the indent grows). According to Eq. (11), the increase in area with depth at constant load is tracked by the parameter ζ_p. Because the indenter has a pyramid shape, one might normally assume that ζ_p should equal to 1. However, it has been demonstrated that ζ_p differs from 1 even for cone-shaped indenters because the area-depth relation depends on the hardness/modulus ratio, which changes during creep.[27] Unlike pyramids, cones have no corners, and the circular

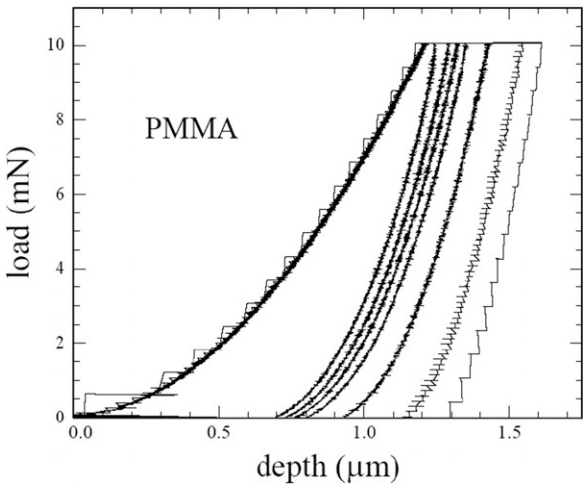

FIG. 2. Load-depth traces for BNC experiments in PMMA, with hold times ranging from 0.05 s to 50 s. The data have been corrected for delays in the electronics using Eq. (8). The discrete steps in load for the longer hold-time experiments are caused by the finite time resolution of the software that controls the load signal.

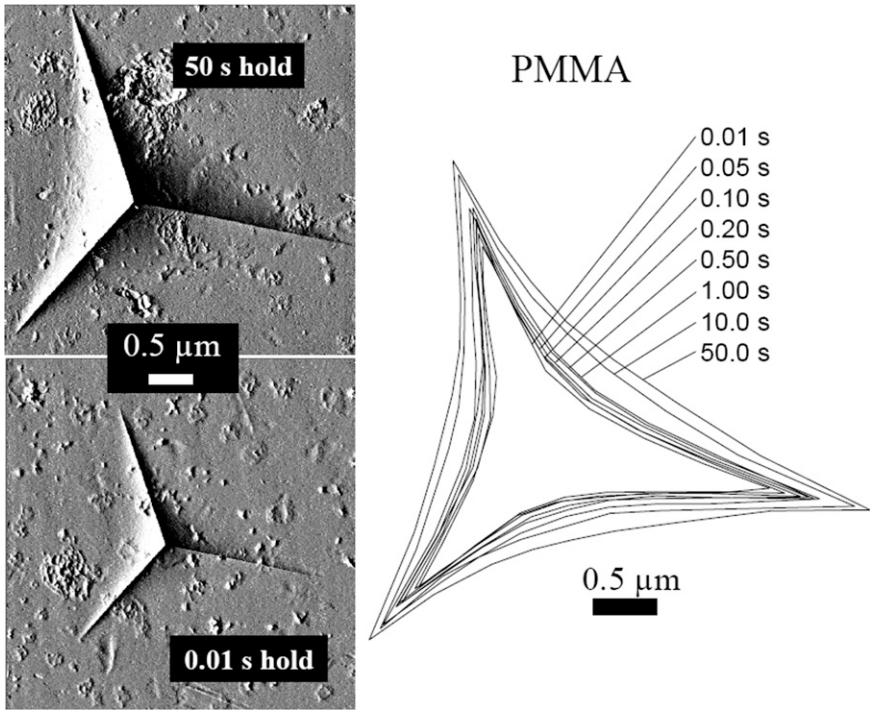

FIG. 3. Images/contours of indents associated with the load-displacement curves in Fig. 2. The indents were all produced under the same loads, but with different creep times. Note that the indent not only grows but changes shape during creep. This shape change is expected as the hardness/modulus drops (see Ref. 26) and is believed to contribute to the value of ζ_p.

shapes of the indents made with cone-shaped indenters will not change depending on the amount of sink-in. In contrast, the shapes of indents made with pyramidal indenters can change depending on the H/E^* ratio. This shape change might affect the value of ζ_p, so that it does not exactly agree with ζ_p for a cone.

Hardness versus strain rate data generated from the experiments on PMMA are shown in Fig. 4. The individual data points represent hardness and strain rate values determined at the ends of the individual creep tests, where it is possible to measure A_0 directly from the image of the indent without having to rely on the approximation in Eq. (11). The lines in this figure are the calculated values of H and $\dot{\varepsilon}_H$, determined from the load-depth-time data of the creep tests using Eqs. (9)–(11). Reasonable agreement between these continuous curves and the individual data points is obtained with $\zeta_p = 1.1$.

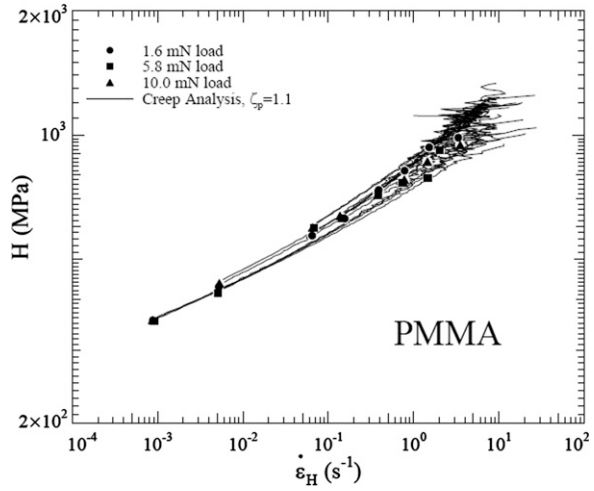

FIG. 4. BNC creep data from PMMA. The individual data points are taken from the ends of the creep tests, where the hardness can be determined directly from the area measurements. The lines are from the analysis of the entire creep hold segment.

B. BMG experiments

As with the PMMA, we measured the areas of indents in the BMGs following creep experiments lasting different lengths of time. These areas were then used to establish the value of ζ_p used for generating hardness-strain rate curves from load-depth-time data. Measured area-time data for Zr54 and Zr45 are compared with $A(t)$, which was generated from Eq. (11) using $\zeta_p = 0.95$, in Fig. 5. The model agrees well with the trend in the measured area-time data.

The $H(\dot{\varepsilon}_H)$ curves collected for the BMGs with t_{creep} = 50 s are shown in Fig. 6. Three different values of P_{max} are represented in the set of curves for each alloy. The data span five orders of magnitude in $\dot{\varepsilon}_H$, over which the hardness decreases 12% for Zr54 and 16% for Zr45. The fact that the curves at different P_{max} closely

resemble each other (save for slight variations in hardness) indicates that the $H(\dot{\varepsilon}_H)$ curves collected by BNC are not affected by the load. Unlike aluminum, which exhibits an indentation size effect in the both the hardness and the rate-dependence of the hardness,[35] these BMGs exhibit no discernable size effects. It should be reemphasized that plastic deformation in materials such as these is often highly inhomogeneous, leading to strain localization and "pop-in" behavior in nanoindentation traces.[36–39] In our experiments, we observe some minor pop-in features in the initial portions of the load versus depth curves (e.g., in the loading data of Fig. 1), and the images of residual indents have morphologies that indicate shear band activity. However, in the $A(t)$ curves of Fig. 5, there are no apparent discontinuities, which allows us to analyze the creep data under the assumption that deformation is homogenous.

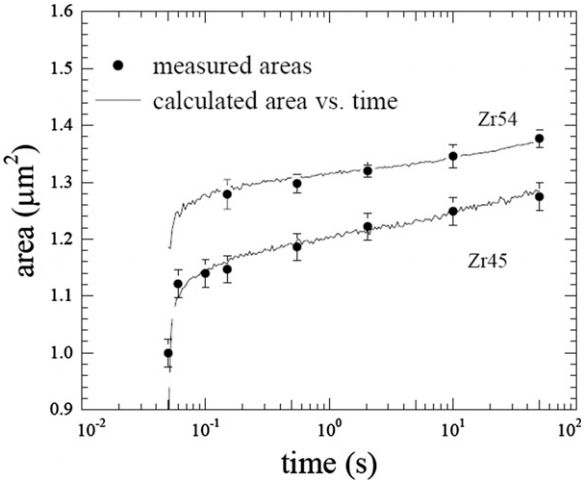

FIG. 5. A comparison of experimentally-determined indent areas (discrete data), taken from creep experiments lasting for different lengths of time, with the areas predicted from Eq. (11) (continuous data). Both the Zr54 and Zr45 data are well represented by the power law exponent $\zeta_p = 0.95$.

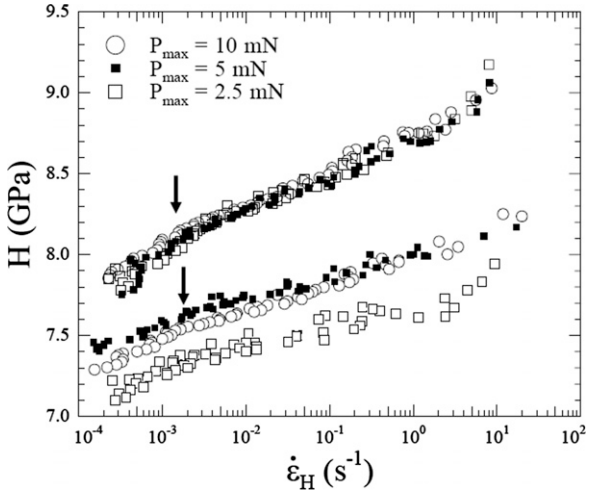

FIG. 6. $H(\dot{\varepsilon}_H)$ curves for the two BMG specimens. The data span five orders of magnitude in strain rate. The slopes of these curves are the strain rate sensitivity of the hardness, m_H. The properties appear to be independent of load. Arrows indicate strain rates at which a change in mechanism appears to take place.

The experimental results show anomalous behavior at low strain rates, however, where the $H(\dot{\varepsilon}_H)$ curves go from being generally concave up to concave down. These transitions occur at locations indicated by the arrows in Fig. 6. The concave up behavior is characteristic of a kinetic law of the form of Eq. (2), governed by a stress-dependent activation energy of the form of Eq. (4). This departure from the concave upward shape at low strain rates might be related to pop-in or shear-banding behavior,[36–39] because we observe the characteristic discontinuities in the loading portions of our load-depth curves become more prominent at low loading rates. We do not observe any significant displacement burst activity during constant-load creep. Nevertheless, these anomalous low-strain-rate data were excluded from further analysis.

The results of the supplementary experiments to examine path-dependence of deformation in Zr54 are presented in Fig. 7. The open circles are the $H(\dot{\varepsilon}_H)$ data for the 50 s BNC experiment, taken from Fig. 6. The other symbols are for the three different creep tests with segment times of equal length (trapezoid loading profiles, shown inset). As with the BNC data of Fig. 6,

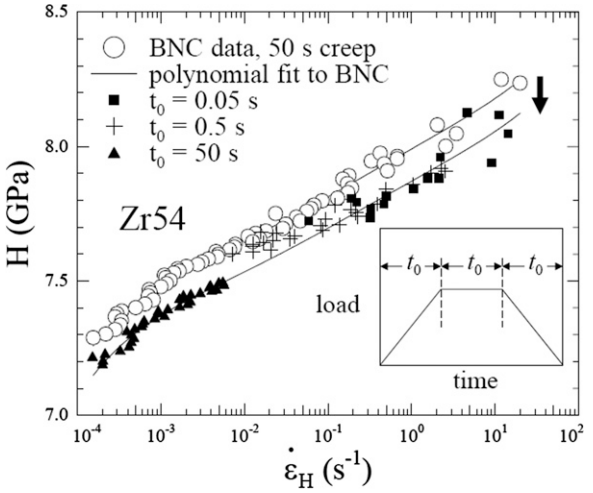

FIG. 7. A comparison of the supplemental experiments performed on Zr54 to explore the effects of loading history on measured properties. Supplemental load profiles all have the same shape except that the timescales are different. In contrast, the BNC data have a load profile with 0.05 s loading and 50 s creep. The lines are fifth-order polynomial fits to the BNC data, with the lower curve shifted down by 0.2 GPa for clarity purposes (arrow). The data from creep experiments with trapezoidal loading profiles have been shifted vertically by small amounts (corresponding to the uncertainty in area) to get them to overlap. Comparison demonstrates that the results are independent of initial loading rate.

the creep data in Fig. 7 from these supplementary experiments were generated using the constant-load segment of the test. The three data sets in Fig. 7 have been shifted with respect to each other by small amounts in hardness (so that they overlap), consistent with uncertainty in the measured areas at the end of creep. This composite curve has also been shifted down in hardness (arrow) from the BNC data, for illustration purposes. Taken together, these three sets of data closely reproduce the entire BNC curve, even though they were generated from tests that have loading rates differing by as much as a factor of 1000. The results indicate that the data collected during BNC are relatively path-independent across the range of strain rates tested, and that the instantaneous hardness at a given value of strain rate does not depend upon the initial loading rate.

V. DISCUSSION

A. Conversion of $H(\dot{\varepsilon}_H)$ curves to $\sigma(\dot{\varepsilon})$ curves

To properly interpret BNC data, it helps to transform hardness into uniaxial flow stress and indentation strain rate into uniaxial strain rate. In the case of PMMA, this transformation allows us to directly compare our data with data acquired by conventional means.[15,23] The transformation of hardness to flow stress is known from Johnson's analysis.[40] The transformation of strain rate entails conversion of m_H into m_σ then integration of $1/m_\sigma$. Plastic deformation in PMMA and BMGs is known to be pressure sensitive, but in employing these transformations we initially neglect the role of hydrostatic stress on yielding and use transformations that are known to govern von Mises materials. The role of hydrostatic stress is then examined using the activation volume concept introduced in Eq. (3).

The ratio of hardness to yield stress (k) is plotted as a dashed curve against H/E^* in Fig. 8 for finite element analysis of rate-sensitive von Mises materials indented by a frictionless cone. The ratio k is "universal" in the sense that it is independent of work hardening and strain rate sensitivity properties and only depends on H/E^*.[26] For a frictionless indenter, k saturates at about 2.6 at low H/E^*, but in the presence of friction this limit increases to about 3. The solid line in Fig. 8 is derived from experimental data presented by Johnson,[40] which take friction into account. According to finite element simulations of von Mises materials, conversion of m_H to m_σ is accomplished by the formula[26,27]

$$\frac{m_H}{m_\sigma} \approx \sqrt{1-(x/0.21)^2} \times \left[0.91 - 0.057 \arctan\left(\frac{\log(x/28.2)}{0.2}\right)\right] , \quad (12)$$

where $x = H/E^*$. This transformation remains valid independent of work hardening, strain rate sensitivity, and specimen-indenter friction.[26,41]

B. Analysis of PMMA BNC data

The conversion of an $H(\dot{\varepsilon}_H)$ curve into a $\sigma(\dot{\varepsilon})$ curve proceeds in three steps. The first step is to convert hardness to flow stress by using the solid curve in Fig. 8. The resulting $\sigma(\dot{\varepsilon}_H)$ curve is shown as the solid line in Fig. 9. Notice that on the log(stress) scale, the $\sigma(\dot{\varepsilon}_H)$ curve is not parallel to the $H(\dot{\varepsilon}_H)$ curve. This is because the proportionality factor k is not constant, but instead varies with H/E^*.

The next step is to calculate m_σ from m_H. Both of the strain rate sensitivities are shown in Fig. 10. m_H has been

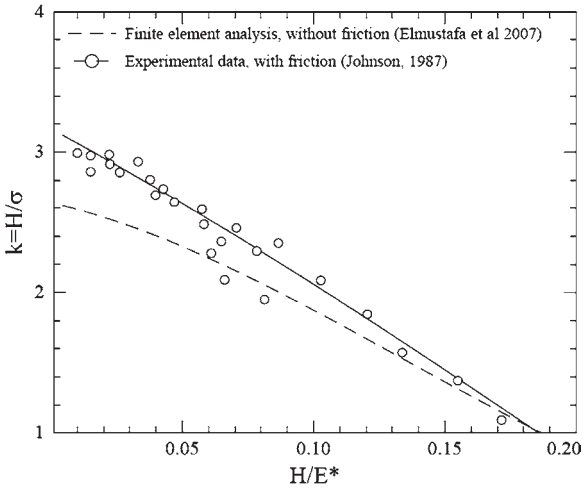

FIG. 8. Variation of hardness/yield stress ratio as a function of hardness indentation modulus, based on Refs. 26 and 40. The dashed curve takes into account the presence of specimen-indenter friction and is used in the analysis of the experimental data.

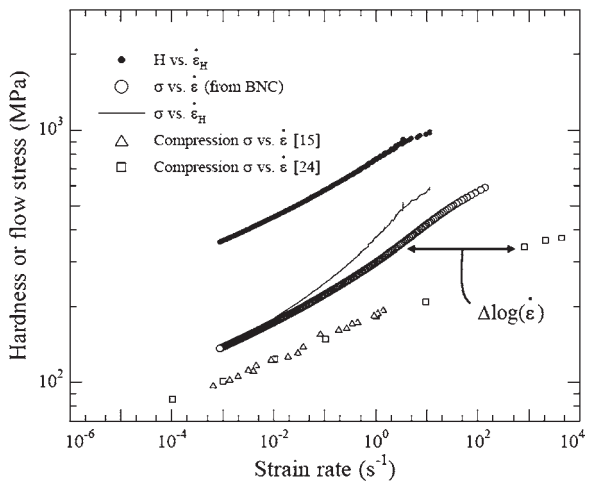

FIG. 9. Conversion of $H(\dot{\varepsilon}_H)$ data to the derived $\sigma(\dot{\varepsilon})$ curve, and comparison between this curve with literature compression data for the flow stress. $\Delta\log(\dot{\varepsilon})$ refers to the shift distance used in Fig. 10 to estimate pressure activation volume.

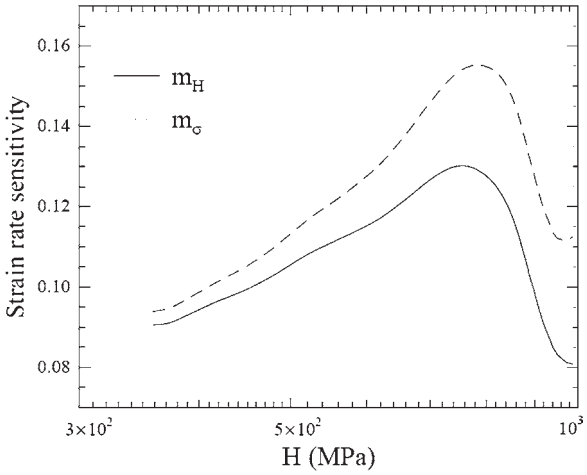

FIG. 10. Conversion of m_H to m_σ using Eq. (11), as an intermediate step in constructing the $\sigma(\dot{\varepsilon})$ curve in Fig. 8.

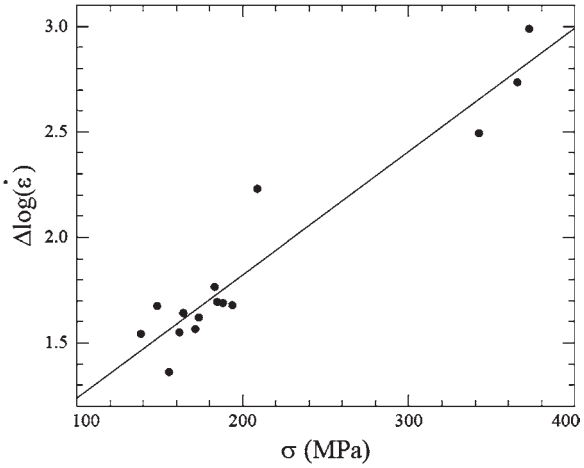

FIG. 11. Shift distance (indicated in Fig. 8) as a function of σ. The slope of the line provides an estimate of V_h*.

obtained from the derivative of a spline fit to the $H(\dot{\varepsilon}_H)$ data in Fig. 9, whereas m_σ has been generated from m_H using the conversion in Eq. (12) and taking into account how H/E* changes throughout the data. It is assumed that the conversion for a pressure sensitive material is approximately the same as for a von Mises material.

The last step is to integrate $1/m_\sigma$ against log σ. In Fig. 9, the integration is horizontal rather than the usual vertical integration. The constant of integration in this procedure is unknown, so we arbitrarily choose it to be zero, recognizing that there is an unknown horizontal shift associated with the $\sigma(\dot{\varepsilon})$ data generated from the indentation test. The generated curve is shown using open circles in Fig. 9.

From an inspection of Fig. 9, it instantly becomes obvious that the converted $\sigma(\dot{\varepsilon})$ curve based on BNC has a different shape from the literature $\sigma(\dot{\varepsilon})$ data obtained using uniaxial compression. The difference is likely caused by the influence of the hydrostatic stress on the yielding of PMMA. The role of hydrostatic stress is dramatically revealed in the measured H values (see Fig. 4) that approach or exceed 1 GPa at strain rates of about 10 s^{-1}. If, by comparison, we extrapolate based on the uniaxial data in Fig. 9, then to achieve similar levels of stress in a uniaxial experiment would require strain rates of 10^6–10^8 s^{-1}. By virtue of Eqs. (2) and (3b), the effect of σ_h is to shift the deformation rate toward lower strain rates by an amount

$$\Delta \ln \dot{\varepsilon} \approx \frac{V_h^*}{k_B T} \Delta\sigma_h \quad . \tag{13}$$

In Fig. 11 we show the horizontal shift distance required to move the hardness-generated $\sigma(\dot{\varepsilon})$ data on top of the uniaxial $\sigma(\dot{\varepsilon})$ curve (indicated in Fig. 9 by the double arrow). The difference between the hydrostatic stresses in the hardness tests and uniaxial tests are on the order of σ, so the slope of the line formed by the data ($\sim 5.8 \pm 0.5$ GPa^{-1}) provides an estimate of the pressure activation volume: $V_h^* \approx 0.055$ nm^3. This measured value is the correct order of magnitude: it is about a factor of 2 smaller than pressure activation volumes reported for polyethylene and poly-(tetrafluoroethylene) at similar pressure levels.[42,43] A rather modest pressure effect can therefore explain the difference between the hardness and compression data in PMMA.

In conclusion, $H(\dot{\varepsilon}_H)$ data are transformed into $\sigma(\dot{\varepsilon})$ data based on the approximation that the $H \rightarrow \sigma$ and $m_H \rightarrow m_\sigma$ conversions are the same for pressure-sensitive PMMA as for previously modeled von Mises materials. In the converted indentation data, the observed strain rates at high stress are lower than would be anticipated from an extrapolation of the uniaxial data. The discrepancy can be accounted for based on a pressure activation volume.

C. Analysis of BMG BNC data

Because the drop in hardness for the BMG specimens during creep is much smaller than that of the PMMA, the BMG data are comparatively noisy and cannot be analyzed using the same methods as chosen for PMMA. We are nevertheless able to examine the form of $\Delta G(\tau)$, along with the other parameters in Eqs. (2), (3a), and (4), under the assumption that deformation is homogenous, as described previously.

Deformation in a metallic glass by the operation of STZs is primarily responsive to shear stresses, so we first convert the hardness to shear flow stress. Again, we neglect the pressure sensitivity of yielding in this conversion. After the analysis, we can then go back and estimate the effect of the pressure activation volume on the flow behavior of the material. The ratio of hardness to flow stress in BMGs is generally higher than for von Mises materials. For metallic glasses in our hardness range, $H/\sigma \approx 3$, according to the data in Schuh et al. and

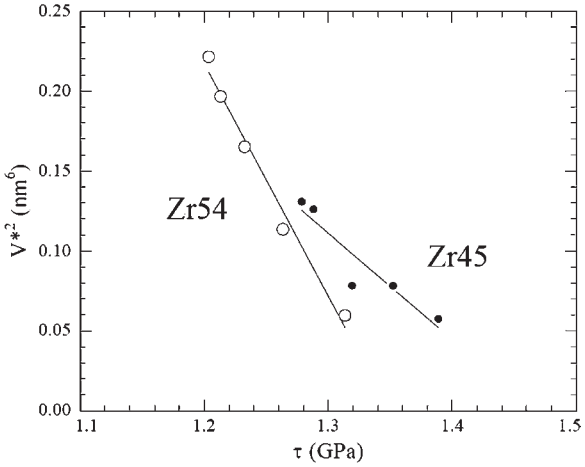

FIG. 12. Activation volume data generated using the BNC curves for the BMGs. From these data, all of the parameters for the thermal activation model [from Eqs. (2) and (4)] can be estimated.

Prasad et al.[44,45] If the metallic glasses were von Mises materials, H/σ would be about 2.6 for the same H/E^* ratios. The ratio of the imposed stress σ to the shear stress τ is about 2 in a compression test, so $H/\tau \approx 6$ for these alloys. From the resulting $\tau(\dot{\varepsilon}_H)$ curve, the $V_\tau^*(\tau)$ data may be calculated from Eq. (3a), recognizing the fact that m_H must be transformed to m_τ. We approximate $m_\tau = m_\sigma$, assuming, for the moment, that σ_h does not influence the strain rate.

A linear relationship is found when $\left[V_\tau^*(\tau)\right]^2$ is plotted against τ, as shown in Fig. 12, indicating that the data are consistent with a power law activation energy of the form of Eq. (4), with $n = 3/2$. (In practice, a range of n between 3/2 and 2 can be fit to the data, but for the present we use $n = 3/2$.) If extrapolated to low stresses the data can be used to estimate $V_\tau^*(0) = 1.4 \pm 0.1$ nm^3 for Zr54 and 1.0 ± 0.1 nm^3 for Zr45. The limiting flow stress (τ_c) at 0 K can be determined from the intercepts of the lines in Fig. 12 with the τ-axis. Using $n = 3/2$, the activation energy at zero stress can be estimated for each BMG from the intercepts of the curves in Fig. 12 with the V_τ^*-axis, because $V_\tau^*(0) = 3\Delta G_0/2\tau_c$. The derived activation parameters for the two BMGs are listed in Table I.

Johnson et al.[14] have proposed a cooperative shear model for the flow of metallic glasses. From their free energy function, with $n = 3/2$, and substituting in their estimates for the parameters, the extrapolation of V_τ^* at high stresses to $\tau = 0$ results in

$$V_\tau^*(0) \approx 7\gamma_c\Omega_{STZ} \quad , \qquad (14)$$

where Ω_{STZ} is the volume of a shear transformation zone and γ_c is the strain experienced by an STZ during activation at $\tau = 0$. We therefore estimate from their model and our data $\gamma_c\Omega_{STZ} \approx 0.20$ nm^3 for Zr54 and 0.14 nm^3 for Zr45. Measurements have been made of $\gamma_c\Omega_{STZ}$ using high temperature compression creep in a Pd-based BMG[46] and high temperature nanoindentation on an Au-based BMG.[47] These experiments yield values of 0.106 and 0.19 nm^3, respectively. Our estimates, which are based on low-temperature deformation, are similar.

TABLE I. Activation parameters for BMGs determined from BNC.

Alloy	τ_c (GPa)	ΔG_0 (eV)	$\dot{\varepsilon}_0$ (s–1)
Zr54 ($Zr_{54}Cu_{38}Al_8$)	1.35 ± 0.01	7.9 ± 0.6	1.4×10^7
Zr45 ($Zr_{45}Cu_{49}Al_6$)	1.45 ± 0.03	6.0 ± 0.7	3×10^6

Using the values of τ_c and ΔG_0 in Table I, the final unknown deformation parameter, $\dot{\varepsilon}_0$, is determined from a fit of the $\tau(\dot{\varepsilon})$ data to Eq. (2). These values are somewhat smaller than expected, since the rate parameter should be of the order: (*STZ concentration*) × (*atomic vibrational frequency*) × (*shear strain in an STZ*) $\approx 0.01 \times 10^{13}$ s^{-1} $\times$ 0.01 $\approx 10^9$ s^{-1}. However, as is the case for PMMA, hydrostatic stress effects will suppress deformation, and the inclusion of a hydrostatic term in the activation energy would produce larger values of $\dot{\varepsilon}_0$.

VI. CONCLUSION

We have applied a novel indentation test technique, broadband nanoindentation creep, to measure the strain-rate-dependence of the hardness in two Zr-Cu-Al bulk metallic glasses and amorphous poly-(methyl methacrylate). The resulting hardness-versus-strain rate data span five orders of magnitude in strain rate for the metallic glasses and four orders of magnitude for PMMA. Using these data, we have been able to examine the relationship between creep data obtained from indentation and yield stress-strain rate data obtained from uniaxial compression tests of PMMA. The main difference between the two arises unambiguously from the effects of hydrostatic stress on thermally activated deformation of PMMA. We have also used BNC data to determine the set of activation parameters for deformation of the Zr-based glasses, and find indications that there is a hydrostatic component affecting these data as well.

ACKNOWLEDGMENTS

The authors gratefully acknowledge Y. Austin Chang, for the access to his suction casting facilities. Additional thanks go to Oden Warren, Lance Kuhn, and the rest of the staff of the Hysitron Minneapolis Lab, for technical details on the Triboindenter. This research was sponsored by the National Science Foundation under Award CMS-0528073.

REFERENCES

1. M.R. VanLandingham: Review of instrumented indentation. *J. Res. Nat. Inst. Stand. Technol.* **108,** 249 (2003).

2. D. Newey, M.A. Wilkins, and H.M. Pollock: An ultra-low-load penetration hardness tester. *J. Phys. E: Sci. Instrum.* **15,** 119 (1982).
3. J.B. Pethica, R. Hutchings, and W.C. Oliver: Hardness measurement at penetration depths as small as 20 nm. *Philos. Mag. A* **48,** 593 (1983).
4. S.-P. Hannula, D. Stone, and C.-Y. Li: Determination of time-dependent plastic properties by indentation load relaxation techniques, in *Electronic Packaging Materials Science*, edited by E.A. Giess, K-N. Tu, and D.R. Uhlmann (Mater. Res. Soc. Symp. Proc. **40,** Pittsburgh, PA, 1985), pp. 217–224.
5. P.M. Sargent and M.F. Ashby: Indentation creep. *Mater. Sci. Technol.* **8,** 594 (1992).
6. W.B. Li and R. Warren: A model for nanoindentation creep. *Acta Metall. Mater.* **41,** 3065 (1993).
7. A.F. Bower, N.A. Fleck, A. Needleman, and N. Ogbonna: Indentation of a power law creeping solid. *Proc. R. Soc. London, Ser. A* **441,** 97 (1993).
8. D.S. Stone and K.B. Yoder: Division of the hardness of molybdenum into rate-dependent and rate-independent parts. *J. Mater. Res.* **9,** 2524 (1994).
9. S. Yang, Y-W. Zhang, and K. Zeng: Analysis of nanoindentation creep for polymeric materials. *J. Appl. Phys.* **95,** 3655 (2003).
10. A.C. Fischer-Cripps: A simple phenomenological approach to nanoindentation creep. *Mater. Sci. Eng., A* **385,** 74 (2004).
11. D.L. Goldsby, A. Rar, G.M. Pharr, and T.E. Tullis: Nanoindentation creep of quartz, with implications for rate- and state-variable friction laws relevant to earthquake mechanics. *J. Mater. Res.* **19,** 357 (2004).
12. M.F. Ashby and H.J. Frost: The kinetics of plastic deformation above 0°K, in *Constitutive Equations in Plasticity*, edited by A.S. Argon (MIT Press, Cambridge, MA, 1975), p. 119.
13. P. Haasen: *Physical Metallurgy*, 3rd ed., translated by Janet Mordike (Cambridge University Press, Cambridge, UK, 1996), pp. 289–292.
14. W.L. Johnson and K. Samwer: A universal criterion for plastic yielding of metallic glasses with a $T/T_g^{2/3}$ temperature dependence. *Phys. Rev. Lett.* **95,** 195501 (2005).
15. G.M. Swallowe and S.F. Lee: A study of the mechanical properties of PMMA and PS at strain rates of 10^{-4} to 10^{3} over the temperature range 293–363 K. *J. Phys. IV* **110,** 33 (2003).
16. J.W. Christian: *The Theory of Transformations in Metals and Alloys*, 2nd ed. (Pergamon Press, Oxford, UK, 1975), p. 81.
17. F. Spaepen: Defects in amorphous metals, in *Les Houches Lectures XXXV: Physics of Defects*, R. Balian (North Holland Press, Amsterdam, 1981), p. 133.
18. C.A. Schuh, T.C. Hufnagel, and U. Ramamurty: Mechanical behavior of amorphous alloys. *Acta Mater.* **55,** 4067 (2007).
19. A.S. Argon: Plastic deformation in metallic glasses. *Acta Metall.* **27,** 47 (1979).
20. M.L. Falk and J.S. Langer: Dynamics of viscoplastic deformation in amorphous solids. *Phys. Rev. E* **57,** 7192 (1998).
21. J.D. Eshelby: The determination of the elastic field of an ellipsoidal inclusion, and related problems. *Proc. R. Soc. London, Ser. A* **241,** 376 (1957).
22. B.E. Read: Dynamic mechanical and creep studies of PMMA in the α- and β-relaxation regions. Physical ageing effects and non-linear behaviour, in *Lecture Notes in Physics, Vol. 277: Molecular Dynamics and Relaxation Phenomena in Glasses*, edited by T. Dorfmüller and G. Williams (Springer-Verlag, Berlin, 1987), p. 61.
23. J. Richeton, S. Ahzi, K.S. Vecchio, F.C. Jiang, and R.R. Adharapurapu: Influence of temperature and strain rate on the mechanical behavior of three amorphous polymers: Characterization and modeling of the compressive yield stress. *Int. J. Solids Struct.* **43,** 2318 (2006).
24. J.J. Gilman: Flow via dislocations in ideal glass. *J. Appl. Phys.* **44,** 675 (1973).
25. J.D. Eshelby: The continuum theory of lattice defects. *Solid State Phys.* **3,** 79 (1956).
26. A.A. Elmustafa, S. Kose, and D.S. Stone: The strain-rate sensitivity of the hardness in indentation creep. *J. Mater. Res.* **22,** 926 (2007).
27. D.S. Stone and A.A. Elmustafa: Analysis of indentation creep, in *Fundamentals of Nanoindentation and Nanotribology IV*, edited by E. Le Bourhis, D.J. Morris, M.L. Oyen, R. Schwaiger, and T. Staedler (Mater. Res. Soc. Symp. Proc. **1049,** Warrendale, PA, 2008), pp. 163, 1049-AA10-02.
28. H. Cao, D. Ma, K-C. Hsieh, L. Ding, W.G. Stratton, P.M. Voyles, Y. Pan, M. Cai, J.T. Dickinson, and Y.A. Chang: Computational thermodynamics to identify Zr-Ti-Ni-Cu-Al alloys with high glass-forming ability. *Acta Mater.* **54,** 2975 (2006).
29. J. Hwang and P.M. Voyles: unpublished.
30. J.E. Jakes, C.R. Frihart, J.F. Beecher, R.J. Moon, and D.S. Stone: Experimental method to account for structural compliance in nanoindentation measurements. *J. Mater. Res.* **23,** 1113 (2008).
31. A.H.W. Ngan and B. Tang: Viscoelastic effects during unloading in depth-sensing indentation. *J. Mater. Res.* **17,** 2604 (2002).
32. D. Jang and M. Atzmon: Grain-size dependence of plastic deformation in nanocrystalline Fe. *J. Appl. Phys.* **93,** 9282 (2003).
33. F. Wang, P. Huang, and K.W. Xu: Time dependent plasticity at real nanoscale deformation. *Appl. Phys. Lett.* **90,** 161921 (2007).
34. M.F. Doerner and W.D. Nix: A method for interpreting the data from depth-sensing indentation instruments. *J. Mater. Res.* **1,** 601 (1986).
35. A.A. Elmustafa and D.S. Stone: Nanoindentation and the indentation size effect: Kinetics of deformation and strain gradient plasticity. *J. Mech. Phys. Solids* **51,** 357 (2003).
36. C.A. Schuh and T.G. Nieh: A nanoindentation study of serrated flow in bulk metallic glasses. *Acta Mater.* **51,** 87 (2003).
37. W.H. Li, T.H. Zhang, D.M. Xing, B.C. Wei, Y.R. Wang, and Y.D. Dong: Instrumented indentation study of plastic deformation in bulk metallic glasses. *J. Mater. Res.* **21,** 75 (2006).
38. B. Yang and T.G. Nieh: Effect of the nanoindentation rate on the shear band formation in an Au-based bulk metallic glass. *Acta Mater.* **55,** 295 (2007).
39. C.A. Schuh, A.C. Lund, and T.G. Nieh: New regime of homogeneous flow in the deformation map of metallic glasses: Elevated temperature nanoindentation experiments and mechanistic modeling. *Acta Mater.* **52,** 5879 (2004).
40. K.L. Johnson: *Contact Mechanics* (Cambridge University Press, Cambridge, UK, 1987), pp. 153–241.
41. A.A. Elmustafa and D.S. Stone: Strain rate sensitivity in the nanoindentation creep of hard materials. *J. Mater. Res.* **22,** 2912 (2007).
42. L.A. Davis and C.A. Pampillo: Deformation of polyethylene at high pressure. *J. Appl. Phys.* **42,** 4659 (1971).
43. L.A. Davis and C.A. Pampillo: Kinetics of deformation of PTFE at high pressure. *J. Appl. Phys.* **43,** 4285 (1972).
44. C.A. Schuh and T.G. Nieh: A survey of instrumented indentation studies on metallic glasses. *J. Mater. Res.* **19,** 46 (2004).
45. K.E. Prasad, R. Raghavan, and U. Ramamurty: Temperature dependence of pressure sensitivity in a metallic glass. *Scr. Mater.* **57,** 121 (2007).
46. M. Heggen, F. Spaepen, and M. Feuerbacher: Creation and annihilation of free volume during homogeneous flow of a metallic glass. *Mater. Sci. Eng., A* **1186 375–377,** (2004).
47. B. Yang, J. Wadsworth, and T.G. Nieh: Thermal activation in Au-based bulk metallic glass characterized by high-temperature nanoindentation. *Appl. Phys. Lett.* **90,** 061911 (2007).